Analysis of the Mw = 4.3 Lorient earthquake sequence: a multidisciplinary approach to the geodynamics of the Armorican Massif, Westernmost France

Julie Perrot, Pierre Arroucau, J. Guilbert, Jacques Déverchère, Y. Mazabraud, Joël Rolet, A. Mocquet, M. Mousseau, L. Matias

Geophys. J. Int. (2005) **162,** 935–950 doi: 10.1111/j.1365-246X.2005.02706.x

Analysis of the Mw 4.3 Lorient earthquake sequence: a multidisciplinary approach to the geodynamics of the Armorican Massif, westernmost France

J. Perrot,[1] P. Arroucau,[2] J. Guilbert,[3] J. Déverchère,[1] Y. Mazabraud,[4] J. Rolet,[1] A. Mocquet,[2] M. Mousseau[1] and L. Matias[5]

[1] *Domaines Océaniques, CNRS, IUEM-UBO, Place Nicolas Copernic,* F-29280 *Plouzané, France. E-mail: jperrot@univ-brest.fr*
[2] *Planétologie et Géodynamique, CNRS, Université de Nantes, BP* 92208, 44322 *Nantes Cedex* 3, *France*
[3] *Laboratoire de Détection et de Géophysique LDG/CEA, BP* 12, F91680 *Bruyères-Le-Châtel, France*
[4] *Géosciences Azur, CNRS, Nice-Sophia Antipolis University, France*
[5] *Centro de Géofisica da Universidade de Lisboa, Campo Grande,* 1749-016 *Lisboa, Portugal*

Accepted 2005 June 6. Received 2005 May 10; in original form 2004 June 23

SUMMARY

A Mw 4.3 earthquake occurred on 2002 September 30, in the Armorican Massif, NW France. Since it was one of the largest events ever recorded in this region, this was the opportunity to improve our seismotectonic knowledge of the Armorican Massif. We performed a post-seismic survey (SISBREIZH), which allowed us to locate accurately 62 aftershocks within 14 days. An analysis of the main shock using broadband records provided a normal fault mechanism with a dextral strike-slip component located at 12-km depth. The aftershock sequence exhibits: (1) a combination of almost pure right-lateral strike-slip and dominant normal faulting similar to the main shock; (2) magnitudes ranging from 0.4 to 1.9 and (3) depths ranging from 11.5 to 13.5 km, that is, close to the main shock hypocenter. The distribution of the aftershocks defines a rupture plane dipping 60° to the south with a fault length of ≈2 km consistent with the source parameters of the main shock. Beside the SISBREIZH survey, a morpho-structural analysis has been conducted: we found fault plane solutions with southward-dipping N120–150 normal fault planes. The stress tensor computed after the aftershock focal mechanisms is a strike-slip regime with a NE–SW extensional direction. The Lorient earthquake appears to reactivate Late Hercynian structures and the whole sequence is reflecting the regional-scale tectonic stress field expressed by a combination of strike-slip and normal faulting.

Key words: Armorican Massif, intraplate seismicity, Lorient earthquake, seismotectonics, stress tensor.

1 INTRODUCTION

On 2002 September 30, a Mw 4.3 earthquake occurred near the city of Lorient, Western France, located in the Southwest Armorican Massif, near the South Armorican Shear Zone (SASZ)(Fig. 1). Since the beginning of the LDG network in 1962, it was one of the largest events recorded by the RéNaSS (Réseau National de Surveillance Sismique, France) and LDG (Laboratoire de Détection et de Géophysique, CEA, France) networks in the Armorican Massif with a magnitude $M_l = 5.7$. The other largest one occurred on 1989 August 21, SW of Brest city, with a magnitude $M_l = 5.0$.

1.1 Geological setting

The Armorican Massif (Fig. 1) is an Upper Proterozoic to Paleozoic basement widely outcropping in northwestern France. It depicts a general EW structural pattern characterized by three domains: the North Armorican Domain (NAD), the Central Armorican Domain (CAD) and the South Armorican Domain (SAD), separated by two main shear zones: the North Armorican (NASZ), and the South Armorican (SASZ) shear zones, respectively (Rolet 1994). The NAD belongs to the Cadomian Orogenic belt, of Upper Proterozoic age (660–450 Myr) (Brun & Bale 1990; Rabu *et al.* 1990), whereas the CAD and the SAD belong to the Variscan belt that developed during the Upper Paleozoic (Brun & Burg 1982; Jegouzo 1980; Ballèvre *et al.* 1994; Shelley & Bossière 2000). The Lorient earthquake occurred in the area where the SASZ splits into two branches: one major shear zone to the north, and another one to the south (Fig. 1).

Since the Paleozoic, the massif has been affected by two main tectonic events:

(1) the Mesozoic extension related to the opening of the Atlantic Ocean (Montadert *et al.* 1977) and

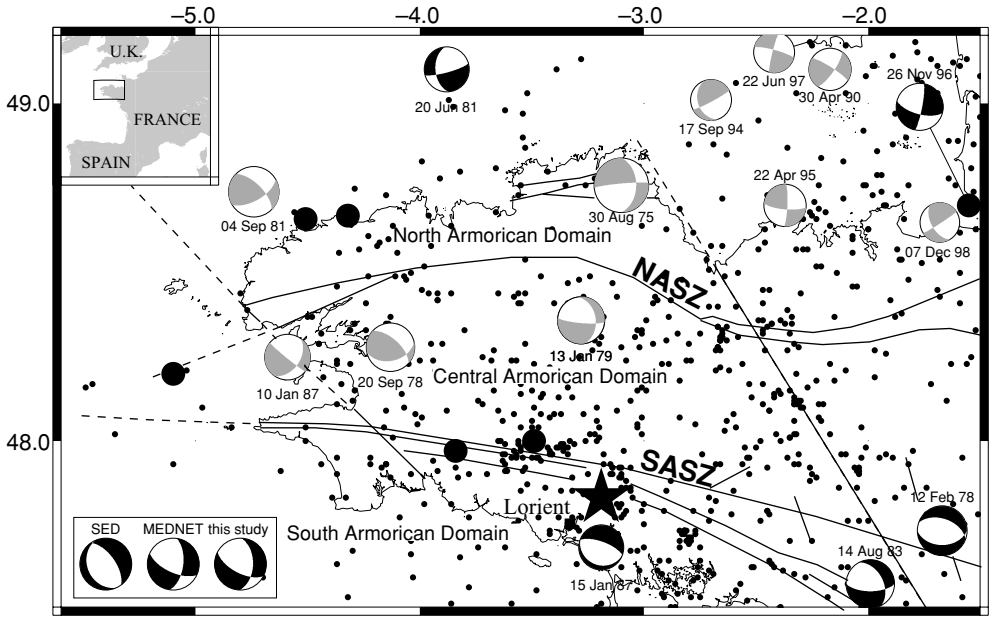

Figure 1. Tectonic sketch map and seismic activity of western Brittany from LDG and RéNaSS database 1962–2003. Inset shows the location of the map within France. The North Armorican Shear Zone (NASZ) and the South Armorican Shear Zone (SASZ) delimit three domains: the North Armorican Domain (NAD), the Central Armorican Domain (CAD) and the South Armorican Domain (SAD). The small and the large circles represent the earthquake in the range of magnitude 2.5 to 4.0, and 4.0 to 5.0, respectively. The focal mechanisms are extracted from the studies by Nicolas *et al.* (1990) for 1975 August 30, 1978 February 12, 1978 September 20, 1979 January 13, 1981 June 20, 1981 September 4, 1983 August 14, 1987 January 10 and 1987 January 15 and by Amorèse *et al.* (2000) for the 1990 April 30, 1994 September 17, 1995 April 22, 1996 November 26, 1997 June 22 and 1998 December 7. The black focal mechanisms are well-constrained solutions and the grey ones are the poorly constrained ones following the authors (Nicolas *et al.* 1990; Amorèse *et al.* 2000). The three focal solutions in the box are solutions given by the Mediterranean Network (MEDNET), the Swiss Earthquake Data centre (SED) and this study for the Lorient earthquake (black star; see Table 1).

(2) a Cenozoic compression related to collision between Europe and Africa (Vigneresse 1988). The Cenozoic deformation of the Armorican Massif is not precisely documented, due to the scarcity of Tertiary deposits. The massif is presently an uplifted intraplate domain of the western European lithosphere, which corresponds to the extended foreland of the Pyrenees and of the Alps (Ziegler *et al.* 1995; Bonnet *et al.* 2000). The rates of relative uplift are still not precisely determined. The observation of large-scale (≈250 km) relief variations and Quaternary river incisions provide values of about 0.05 mm yr^{-1} on a timescale of 10^5 to 10^6 yr (Bonnet *et al.* 1997, 2000), whereas levelling measurements lead to uplift rates in the range 0.2–0.6 mm yr^{-1}, with a maximum value of 1.1 mm yr^{-1}, on a timescale of 100 yr (Lenôtre *et al.* 1999).

1.2 Seismotectonic setting

The seismicity of the Armorican Massif, as detected by the two French permanent networks in the area (LDG and RéNaSS) from 1962 to 2003 (Fig. 1) appears to be rather diffuse. Apparently, there is no close correlation of epicentres to tectonic features, except for some events located on the SASZ. A 3-D model of *P*-wave velocity and *S*-wave seismic anisotropy of the eastern region of the massif shows that the SASZ is a lithospheric structure characterized by a 4–5 per cent velocity contrast, and by a fast shear-wave azimuth parallel to its strike, whereas the NASZ does not show any significant signature at a lithospheric scale (Judenherc *et al.* 2002). This could be related to the differences in the seismic pattern observed between the SASZ and the NASZ.

The magnitude of the events is low to moderate. Eleven events only have reached a magnitude M_l of 4.0 or more since 1962. Earthquakes with magnitudes lower than 4.0 are mainly located in the CAD, probably related to the uplift of the northwestern part of the Armorican Massif. A few seismotectonic studies (Nicolas *et al.* 1990; Amorèse *et al.* 2000) have presented focal mechanisms in the Armorican Massif. Due to its eccentric location, the azimuthal coverage of European seismological networks around the region is poor and multiple solutions exist for most of focal mechanisms (Fig. 1). They tend to show a predominance of strike-slip faulting along subvertical faults. In the northwestern part, faulting is mainly left-lateral along N60°–85° striking faults with some reverse component, whereas in the southern part, near the SASZ, focal mechanisms depict mainly normal faulting striking N90°–130° with a dextral component. These studies indicate horizontal σ_1 (compressional) and σ_3 (extensional) axes roughly striking NW–SE and NE-SW, respectively, in the NAD (Amorèse *et al.* 2000) and in the SAD (Nicolas *et al.* 1990). However, Delouis *et al.* (1993) computed a different stress tensor for the central–western region of France, that is, an area much larger than the Armorican Massif: they obtain a nearly vertical compressional axis σ_1, and conclude that the area is presently in extension in the NE-SW direction combined with strike-slip faulting. A recent study (Mazabraud *et al.* 2005) gives further evidence for a transtensional regime in the South Armorican Massif. Therefore, although the σ_3 axis is generally found to strike NE–SW, the scarcity of fault plane solutions does not allow to describe accurately the stress field in this area.

Various institutions proposed source parameters for the Lorient earthquake (Table 1). The MEDNET (Mediterranean Network) 35-s waveform period solution shows a right-lateral strike-slip solution with a normal component and the SED (Swiss Earthquake Data

Table 1. Proposed source parameters for the Lorient earthquake prior to and from this study.

Source	Latitude	Longitude	Depth	Magnitude	M_o	Str.	Dip	Slip
RéNaSS	47.88	−3.09	10.0	5.4 Ml				
BGS	47.98	−3.23	21.7	4.5 Ml				
LDG	47.83	−3.19	9.6	5.7 Ml		127	61	−127
SED	47.83	−3.20	15.0	4.31 Mw	3.25	156	29	−80
MEDNET	47.82	−3.13	15.0	4.34 Mw	3.7	115	64	−144
This study	47.83	−3.19	12.0	4.27 Mw	2.9	117	62	−133

Depth is in km, Strike (Str.), Dip and Slip are in degrees according to Aki and Richards convention (Aki & Richards 1980). The unit of seismic moment (M_o) is 10^{15} N m. RéNaSS: Réseau National de Surveillance Sismique, France; BGS: British Geological Survey, UK; LDG: Laboratoire de Détection et de Géophysique, CEA, France; SED: Swiss Earthquake Data centre, Switzerland; MEDNET: MEDiterranean NETwork, Italy.

centre) 50-s waveform period solution, a normal fault. A difference in longitude can be also noticed between the MEDNET and the SED location. These differences could be explained by the azimuthal gap of data in the SSW direction of Lorient owing to the presence of the North Atlantic ocean. Although depth values provided by MEDNET and SED are identical (15 km), they appear to be unconstrained in the inversion procedure. The LDG provides a better location of the main shock because the closest station used for this determination is located 12 km away from the epicentre. The focal mechanism solution computed using the FPFIT code (Reasenberg & Oppenheimer 1985) with *P*-waves first motions of LDG and RéNaSS networks is similar to the MEDNET one (Mazabraud *et al.* 2005).

As the seismotectonic pattern is poorly known in this area due to the low seismic activity and sparsity of seismological stations, the Lorient earthquake appears to be a very good opportunity to improve our understanding of the deformation pattern of this intraplate area. Furthermore, as centroid moment tensor determinations are close to the validity limit for a moderate and surficial earthquake, we have installed a dense array of seismic stations two days after the main shock (SISBREIZH campaign) in order to resolve the rupture zone and the post-seismic strain- and stress fields.

From this analysis, we retrieve the source parameters of the Lorient earthquake using the records of the main shock and of the aftershocks. Finally, in order to compare them to the tectonic and stress field around the SASZ, we have conducted, besides the SISBREIZH campaign, a microtectonic field investigation that allows us to relate the seismological results with the structural inheritance of the Lorient area.

2 STRUCTURAL INHERITANCE

The structural analysis is based on two kinds of studies: (1) the identification of the tectonic features as resolved by a 50-m accuracy DEM of the region and (2) a field investigation which aimed at recognizing the direction and the dip of tectonic structures.

2.1 Morpho-structural analysis

On the DEM map (Fig. 2), we can follow the major tectonic directions in the region around the main shock. Three predominant directions are recognized: N110°, N30° and N150°. A ≈N–S direction is also observed if the DEM is illuminated in a N90° direction. All these fractures are inherited from the Hercynian orogeny (Vigneresse 1988). At some places, they are clearly expressed by well-developed morphological fault line scarps, suggesting recent playbacks of these faults, the N30° structures being less visible. The most prominent feature is the triangular shape on the north branch of the SASZ, in the area of the Lorient event, and the system of N150° trending faults on the eastern side between the two branches.

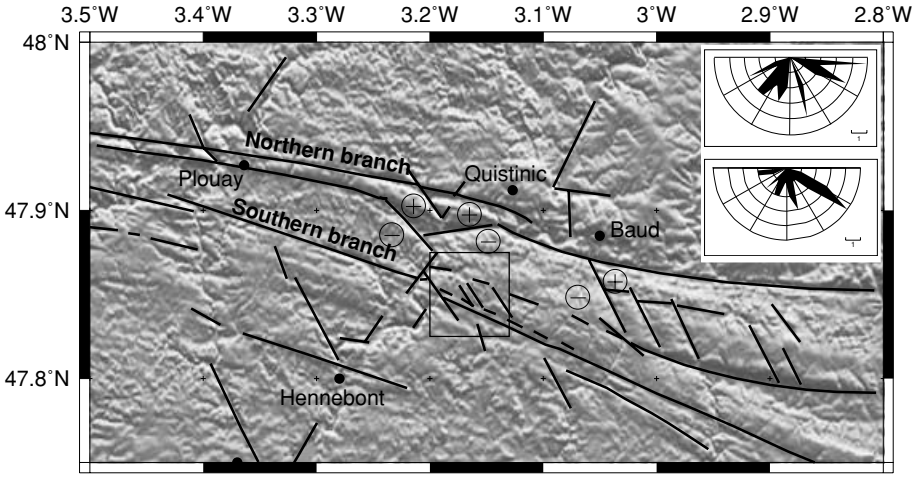

Figure 2. The 50-m-accuracy DEM from IGN (Institut Géographique National) of Lorient earthquake area, showing the northern and southern branch of the SASZ. Fault lineaments have been reported. The DEM is illuminated in a N10° direction. The plus and minus signs represent the relative elevation of fault separated blocks. The square locates the map of Fig. 9. Upper right corner: The upper rose diagram shows the strikes of the fault planes observed on the field and the lower one, the strike of the preferred fault plane solutions obtained from the stress inversion (Fig. 10).

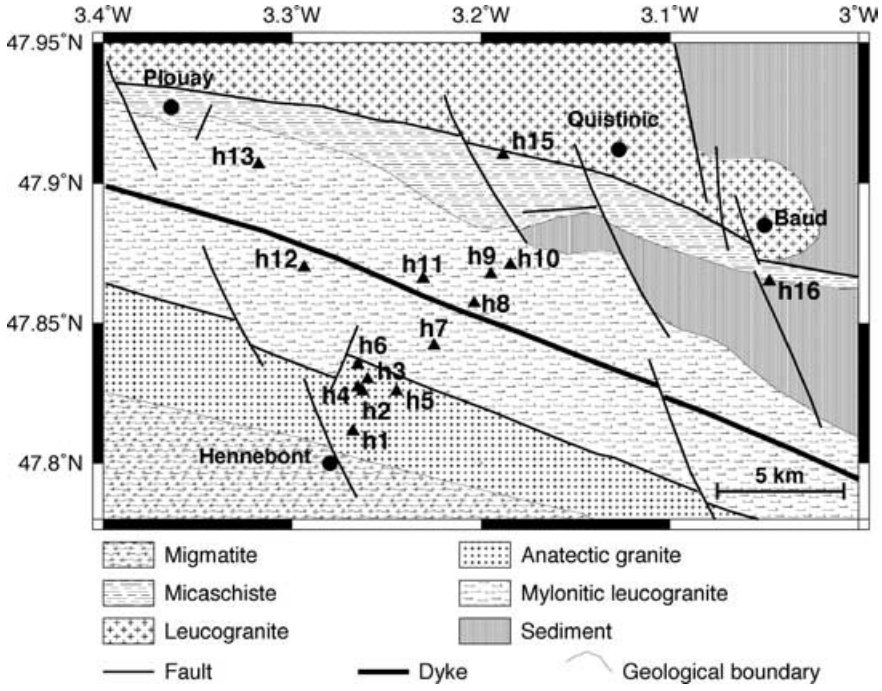

Figure 3. Geological map of the studied area. Triangles indicate the location of the outcrops.

With regard to the regional scale (N110° fault network forming the SASZ), the N150° trending fractures occur as 'en échelon' extensional fault structures formed during dextral shearing. It results into a progressive elevation of the topography on the eastern side of this system. These faults must have played back during an extensive period (probably during the Oligocene), thus explaining their prominent line scarps (Gros & Limasset 1984; Wyns 1991). Finally, relative uplifts of blocks between faults are recognized (Fig. 2), suggesting again recent motions.

2.2 Lorient fault network

Field investigations were carried out in order to characterize the geometry of the faults that have affected the area. Although outcrops are seldom (Fig. 3), 15 sites were identified, and about 100 directions and dips of fault planes were measured. Besides, the geological map has been complemented during the field work (Fig. 3). The most prominent deformations on the outcrops are linked to the compressional Hercynian stress field and to the extensional late-Hercynian deformations. Both of them show ductile deformation features. Nevertheless, other deformations post-dating the Hercynian orogeny are also observed. They show brittle deformation features.

We found that strike-slip faults trending E–W to N120° are dominant, together with the ≈N–S and N30° directions already seen on the DEM (the upper rose diagram in Fig. 2). Dextral strike-slip motions are mostly observed and related to the Hercynian orogeny. Half of the planes show a dip equal to or greater than 75°, showing that the predominant structures in this area are nearly vertical. With 75 per cent of the planes which present a dip larger than 60° (Fig. 4), the present-day attitude of the exposed structures is a steeply dipping fault plane, in good agreement with the SASZ attitude.The fault plane geometry found by the LDG and MEDNET for the Lorient earthquake (with a strike around 120° and a dip angle around 60°) was also identified during the field survey on the Hercynian structure, suggesting a reactivation of these structures.

From this analysis, we therefore deduce strong similaraties between our local scale of observation and the regional one: four main tectonic directions have been recognized in both studies (N–S, N30°, N110°, N150°, all inherited from the Hercynian period). The fault plane geometry found by the LDG and MEDNET were also identified during the field survey in the Lorient area on an Hercynian structure, suggesting a reactivation of the SASZ.

3 SOURCE PARAMETERS OF THE MAIN SHOCK

The Lorient earthquake occurred on 2002 September 30, at 6h44 GMT. In order to determine its depth and its source parameters, we adopt different approaches using records at global and regional scales.

3.1 Depth evaluation of the main shock

In order to determine the depth of the main shock, we made a cepstral analysis using the teleseismic records of the Ivory Coast and of the Mongolian arrays. These two sets of data were provided by Lamto Observatory and by Mongolia Academy of Science of Ulaanbaatar, located at 41° and 67° epicentral distances, respectively. The seismometer used in both arrays is a 1-Hz short period ZM500 developed by the LDG. The cepstral analysis is based on the *F*-statistic described by Shumway (1971) and Bonner *et al.* (2002). The objective of the cepstral analysis is to detect echoes in a signal. Coupled with the *F*-statistics, this method allows for the identification of the *pP* and/or the *sP* phases after the *P* arrival by detecting a signal in a set of stationary correlated time series. The analysis of both networks clearly shows that one of the three important peaks for both curves is consistent with a focal depth of 12 ± 2 km (Fig. 5).

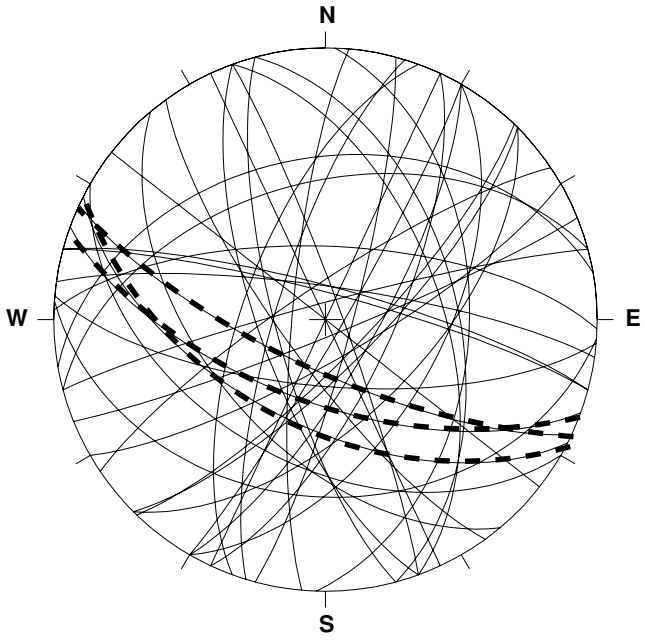

Figure 4. Stereographic projection of the strike and the dip of fault planes surveyed in the Lorient Area. The dashed lines show the strike and dip of fault planes similar to the fault plane solutions found by LDG, MEDNET and our study.

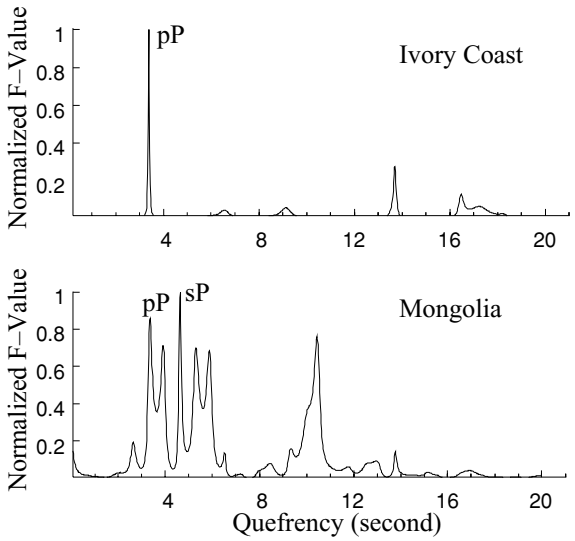

Figure 5. Cepstral *F*-statistics from the Ivory Coast seismic arrays using 5 stations and from the Mongolian seismic network using 6 stations (see location in Fig. 6). The quefrency axis, also called delay axis, represents the time after the *P* arrival. Each peak points at a delay time between the *P*-wave arrival and a coherent second arrival. The differences between the quefrency content of the Ivory and Mongolian arrays are due to the variations in the radiation pattern for both arrays and to a different crustal response under each array. The estimated hypocentral depth with respect to IASPEI model (Kennett 1991) is 12 ± 2 km.

Due to the poor azimuthal coverage and to the small depth value, this evaluation is not robust: a good evaluation of the *pP* and *sP* phases requires a computation over relative amplitudes recorded by several arrays. Nevertheless, we will see in the next subsection that the simulation of the teleseismic waveform confirms this depth estimation (Fig. 6 bottom). Additionally, a free depth estimation at the closest station (QUIF), 12 km away from the epicentre (Fig. 7) gives a depth value of 10 km using a location program equivalent to HYPOINVERSE (Klein 1984). These determinations are mutually consistent and suggest a location of this earthquake within the middle crust, that is, close to the transition of the brittle to the plastic behaviour (Scholz 1990).

3.2 Focal mechanism determination

We first compute the double-couple fault plane solutions using all the available European waveforms from BGS (Bristish Geological Survey, UK), IGN (Instituto Geografico Nacional, Spain), IMP (Instituto de Meteorologia, Portugal), LDG, RéNaSS and SisCaen (réseau sismologique régional de l'Université de Caen, France) networks. The inversion of the *P*-wave first motions using the routine FPFIT (Reasenberg & Oppenheimer 1985) provides the LDG solution reported in Table 1.

In order to test this solution and due to the variability of the available focal mechanisms, we invert the double-couple focal solution using the data recorded at five three-component broadband stations of the LDG network (Fig. 6). The seismometer is a LP-12 type with a flat response in displacement between 2- and 50 s. The focal depth is fixed at 12 km as previously observed with the *P–pP* delay time. The model of propagation is the LDG 1-D velocity crust model (Table 2). Our methodology is based on an iteration grid search over the strike, dip and rake solutions. For each step, we compute the L1 norm for the three components of the five broadband stations in the frequency range 0.1–0.02 Hz (Fig. 6). The Green's functions are computed using the discrete wave number method (Bouchon 1981). The source duration is fixed at 0.4 s. This value is derived from the corner frequency of 2.5 Hz observed on the spectral analysis of short period records of the LDG network.

Fig. 6 shows the comparison between the recorded and the computed waveforms. The computed seismograms using the LDG focal solution give a good fit for the waveforms of the broadband records except for the horizontal components at HAU and ORIF stations which present a misfit in amplitude (Fig. 6). We then obtain by inversion the following focal mechanism solution: strike $= 117^\circ \pm 8^\circ$, dip $= 62^\circ \pm 4^\circ$, rake $= -133^\circ \pm 6^\circ$ and a seismic moment of $2.9\ 10^{15}$ Nm. This solution is consistent with the LDG solution in order to test the validity of this inversion and the focal depth estimation, we compute the teleseismic waveform in Ivory Coast and in Mongolia. Looking at the relative amplitudes and at the delay times between *P*, *pP* and *sP* phases, the simulation (Fig. 6) confirms the focal mechanism obtained by inversion of regional waveforms and the depth value estimated by the cepstral analysis.

For a seismic moment $M_o = 2.9\ 10^{15}$ Nm, we obtain a value of 4.27 for the Mw magnitude, equivalent to those deduced by MEDNET and SED (Table 1). The focal mechanism shows a normal fault with a right-lateral shear component similar to the solution determined by MEDNET. The latter solution is also close to the solution determined by Nicolas *et al.* (1990) for the 1983 earthquake (Fig. 1). The direction of the fault plane is in good agreement with the N110° characteristic fault strike deduced from the structural analysis.

4 AFTERSHOCKS ANALYSIS— SISBREIZH CAMPAIGN

The SISBREIZH post-seismic campaign has been implemented from 2002 October 2 to October 15: 12 stations were installed in a dense network (one station every 7–10 km, Fig. 7) around the preliminary epicentre provided by LDG on September 30. The network consisted of three-component stations equipped with 2 Hz

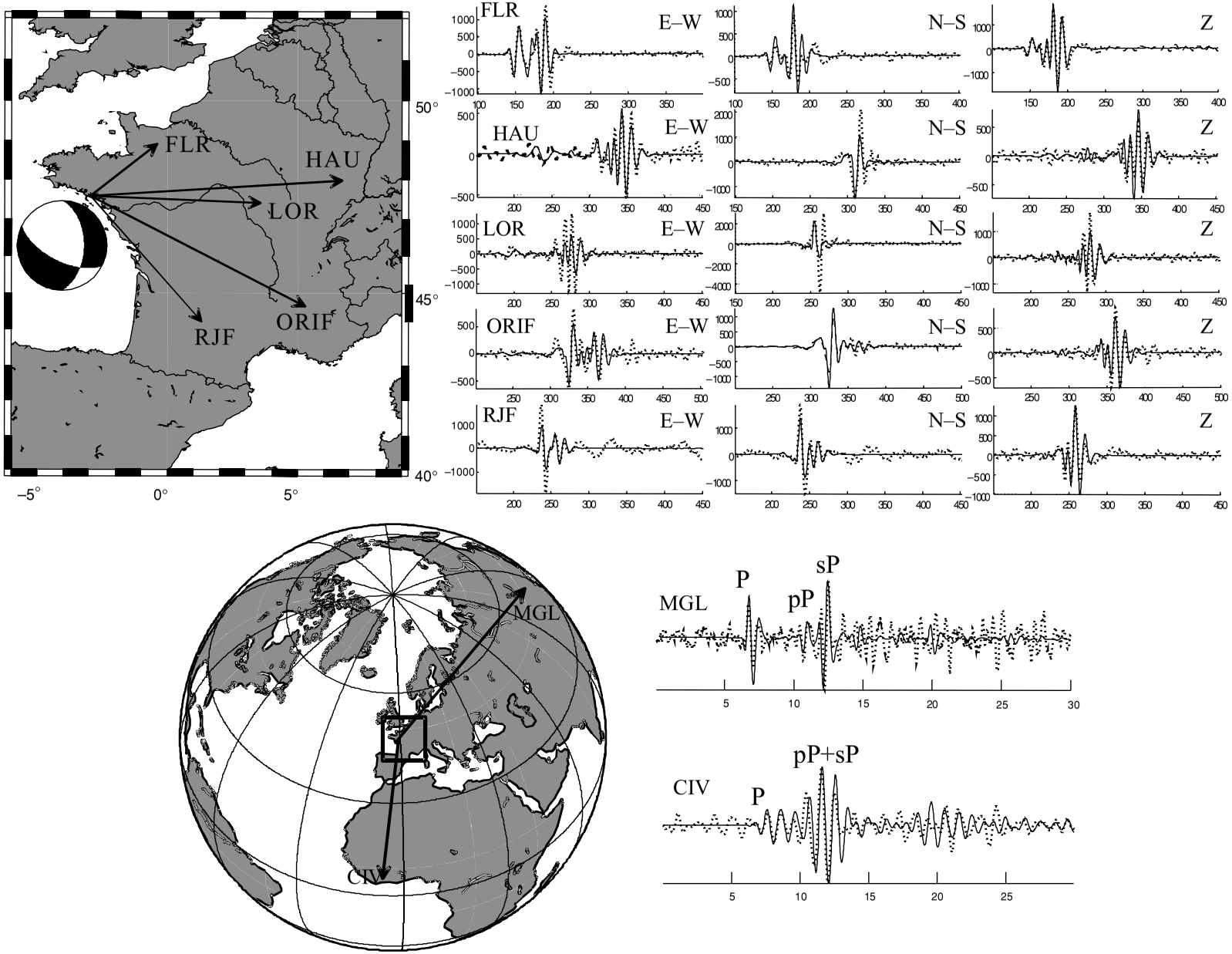

Figure 6. The focal mechanism with strike = 117, dip = 61, rake = −133 and associated waveforms. The solid and dashed curves represent the simulations and the records on the three components, respectively. Timescales are in seconds. The frequency band width is 0.1–0.02 Hz. The depth of the focal mechanism is provided by the *P–pP–sP* delays on the Mongolian record (MGL). The weak *P* amplitude on the Ivory Coast (CIV) record confirm the focal mechanism.

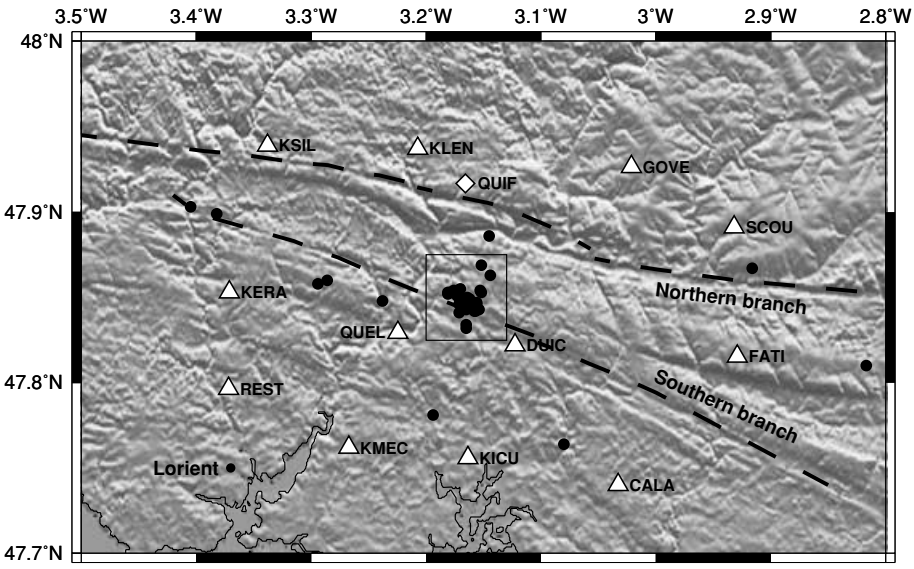

Figure 7. Location of the aftershocks (circles) inside the network. All stations belong to the SISBREIZH temporary network (triangles) except QUIF (diamond) that belongs to the permanent network of the LDG. The square box represents the studied area, and it is the frame of Fig. 8.

short-period sensors of INSU-CNRS (Institut National des Sciences de l'Univers, France) portable network, all connected to GPS antenna for time control. These stations operate in continuous mode with a sampling frequency of 100 Hz. We detect and locate 62 events. The seismograms recorded at the permanent station LDG QUIF (Fig. 7) are also used to improve our solutions for the locations and focal mechanisms of all events.

The seismic activity was important during the first days with about 10 events per day, and it decreased from October 8 until October 15.

4.1 Velocity model

The seismic database has been managed using SEISAN software (Haskov & Ottemöller 1999). We first pick *P* and *S* waves on each of the 62 events and compute their absolute and relative locations using HYPOCENTER (Lienert *et al.* 1986) and hypoDD (Waldahauser & Ellsworth 2000), respectively. The number of phases picked for the 32 selected events with focal mechanisms determined are reported in Table A1. The *P*-wave readings allow us a good picking of their arrival times: we then use a full weight for the location processing. However, as the *S* phases are less clearly readable: we attributed a weight two times smaller for them. Among the 62 events located using HYPOCENTER, 49 are located inside the network (Fig. 7).

The velocity structure under the western part of Brittany is poorly determined. The picked phases are only P_g and S_g phases, and no P_n Moho phases are identified as first arrivals. Only direct rays from the hypocenter to the surface have to be taken into account, and it is therefore not necessary to model the Moho discontinuity in the velocity model. A simple layered model with a constant velocity of 6.00 km s^{-1} gives the smallest average rms (root mean square), that is, 0.041 s, for the 49 events inside the network.

The best fit on a Wadati type diagram provides a V_p/V_s ratio of 1.68. Using these velocity parameters, the mean errors computed in location are 0.7 km and 1.3 km in the horizontal and vertical directions, respectively. The iterative relocation of the aftershocks using hypoDD does not change the hypocenter locations significantly (i.e. less than 200 m and 100 m in the horizontal and vertical directions, respectively). Therefore, all figures and table display the absolute locations of the aftershocks.

Table 2. Velocity model used for the estimation of Green's functions.

Depth (km)	*P* velocity (km s^{-1})	*S* velocity (km s^{-1})
0–0.9	3.00	1.73
0.9–25.9	6.03	3.56
25.9 -	8.16	4.65

4.2 Spatial distribution of the aftershocks

The epicentral map is characterized by a seismic swarm aligned in the N135° azimuth in the middle of the network (Fig. 7). The events located westward of this swarm are located on the SASZ, whereas the others cannot be related to any large-scale known tectonic feature. We report on Fig. 7 the aftershocks from the swarm on a 50 m accuracy DEM (BD Alti IGN, French 'Institut Géographique National'). They occur between the southern branch of the SASZ and a N150 structure, and likely depict the approximate position of the fault plane. The main shock is located 3 km apart from the aftershock swarm in the southwest direction (Fig. 8): this suggests that the actual error on the main shock location is about 3 km using far-field recordings (see Table 1). The fact that this location is computed using only the *P* and *S* wave travel-times of the LDG national records explains this discrepancy.

Two sections crossing the aftershock area are displayed on Fig. 9: one is in the direction of the SASZ (A1B1 in Fig. 8) and another one is perpendicular to this direction (A2B2). All events are located between 11.5 km and 13.5 km in depth (Fig. 9). On section A1B1 (N115°E), two clusters appear: the first one is located at 12 km in the western part of the section and the other one is at 13 km depth in the eastern part. The A2B2 cross-section (N205°E) shows aftershocks trending along a south-dipping plane, with an average dip of 60° (Fig. 9). The same two clusters are also identified on this cross-section. We also project the hypocenters onto: (1) the

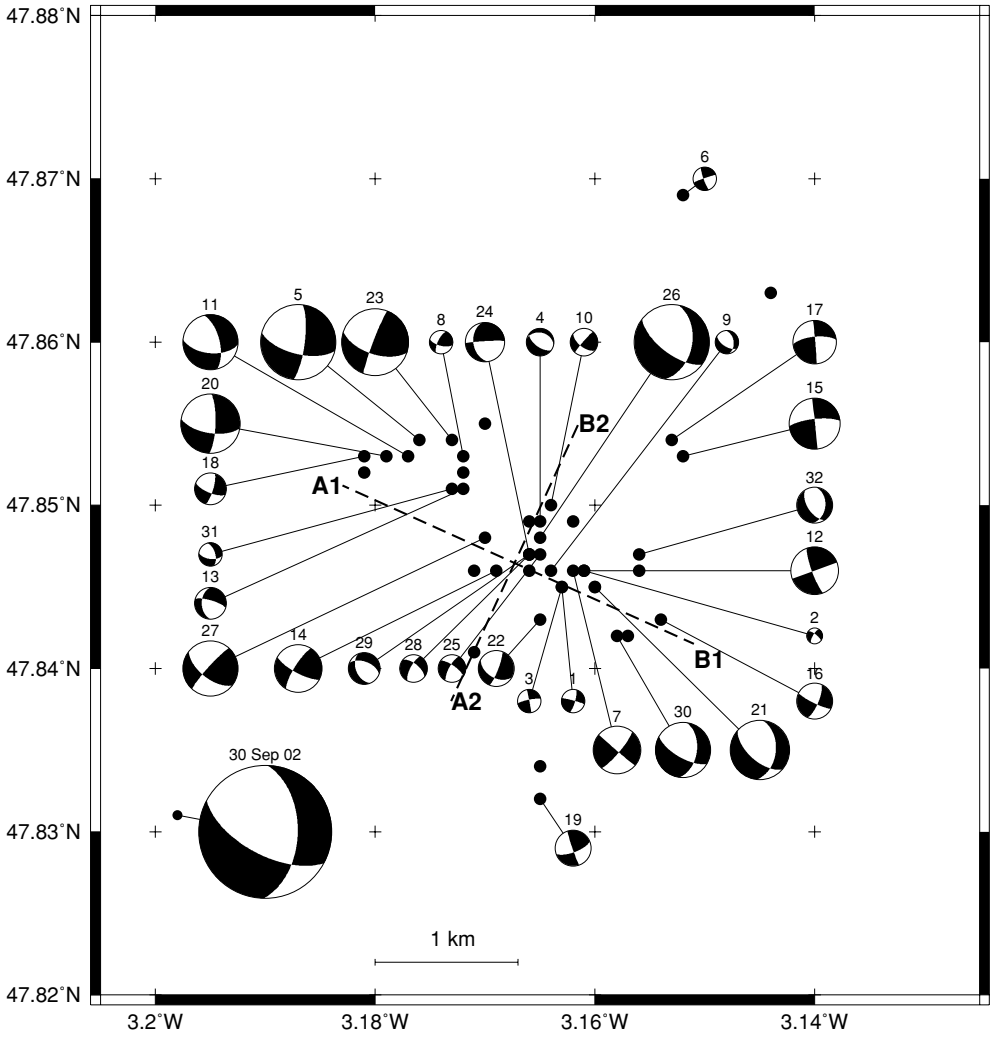

Figure 8. Epicentres and focal mechanisms of the aftershocks. Numbers refer to Table 3. The size of the focal mechanisms is proportional to the magnitude of the events except for the main shock (2002 September 30). The two cross-sections A1B1 and A2B2 are displayed on Fig. 9. The A1B1 cross-section follows the southern branch of the SASZ oriented N115.

mean direction of the aftershock trend (N135°) and (2) the direction perpendicular to this trend (N225°). It appears that the N135° section does not differ significantly from the A1B1 section, whereas a nearly vertical distribution of the events is found on the N225° section. Nevertheless, no N135° tectonic structure has been identified there on the DEM and on field, and nodal planes dipping 60° are statistically more frequent than vertical ones (see next section). Therefore, we will consider that the A2B2 direction better depicts both the hypocenter distribution and the fault dip.

The depth range deduced from the aftershock distribution is consistent with the depth evaluation of the Lorient earthquake using the broadband simulations. It implies that the rupture occurs along an area of stress increase at the base of the upper crust. If we assume a N120° strike with a dip of 60° for the fault plane, a possible structure that has broken during this earthquake is a segment from the northern branch of the SASZ (Fig. 2).

4.3 Assessment of earthquake rupture process

The independently determined values of the corner frequency f_c (2.5 Hz), of the seismic moment M_0 (2.9 10^{15} Nm) and of the aftershock area A (Fig. 9) provide a rather complete description of the earthquake process. The aftershocks distribute over a circular surface with a radius r equal to 1 km (large dashed circle in Fig. 9). Using the value of shear velocity determined in Section 4.1, and assuming a rupture velocity v equal to 3 km s^{-1}, the observed corner frequency corresponds to a value of circular source radius in the range $300 \leq r \leq 532$ m. The lowest and highest values of this range correspond to the dynamic solution of an expanding circular crack model (Madariaga 1976) and to the static solution (Brune 1970), respectively. The quasi-static solution of Sato & Hirasawa (1973) gives $r = 408$ m (small hatched disc in Fig. 9). The aftershock zone thus indicates a larger area than the one activated by the main shock. Following Courboulex *et al.* (1999) who have analysed the rupture of a moderate intraplate event of similar magnitude, we interpret this observation as a reactivation of surrounding fault segments due to a stress increase following the main shock.

By means of the ω^{-2} model (Brune 1970), the corner frequency and the seismic moment also provide a measure of the energy/moment ratio E_S/M_0 (Vassiliou & Kanamori 1982; Kikuchi & Fukao 1988):

$$E_S/M_0 = 2K\pi^3 M_0 f_c^3, \quad (1)$$

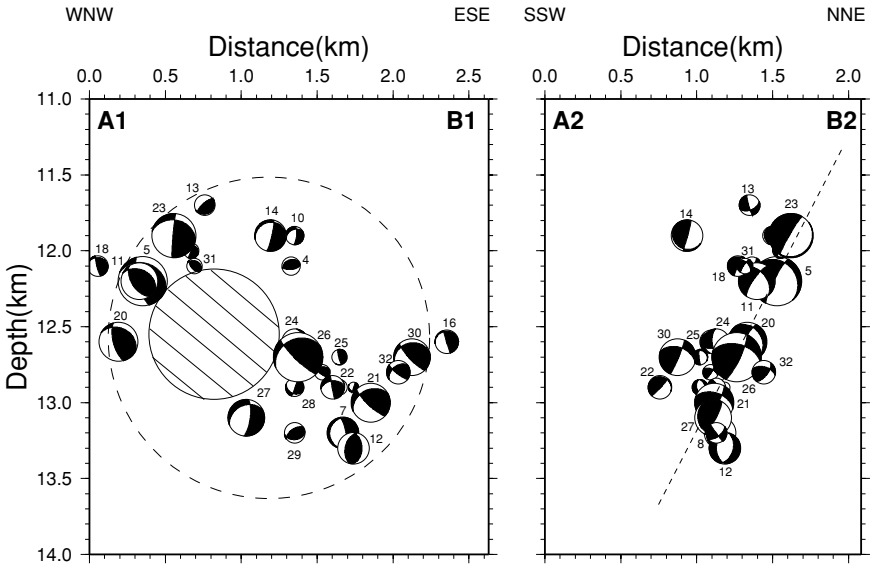

Figure 9. Hypocenter locations along the cross-sections A1B1 and A2B2 of the 32 events focal mechanisms of Fig. 8. The numbers of the focal mechanisms refer to Table 3. In cross-section A1B1, the hatched disc corresponds to the rupture area assessed from the corner frequency of the main shock source. The dashed circle encompasses the region where the stresses induced by the main shock were released in subsequent days. In cross-section A2B2, the aftershocks align along the dip of the main shock fault plane (dashed line). Focal mechanisms are plotted on a vertical plane.

where

$$K = \frac{1}{15\pi\rho V_P^5} + \frac{1}{10\pi\rho V_S^5}. \quad (2)$$

Application of eqs (1) and (2) using the velocities determined in Section 4.1 and a density ρ equal to 2.8 g cm^{-3} gives $E_S/M_0 = 5.77\ 10^{-5}$. The latter value belongs to the range of values ($\sim 5\ 10^{-5}$) which are expected from the energy-magnitude relation of Gutenberg & Richter (1956) for the complete stress drop of a frictionless crack (Kanamori 1977; Kikuchi & Fukao 1988). The ratio E_S/M_0 is related to the strain drop $\overline{\Delta\sigma}/2\mu$ by

$$E_S/M_0 = \eta\Delta\overline{\sigma}/2\mu, \quad (3)$$

where η is the seismic efficiency and μ is the rigidity ($\mu \sim 3.57\ 10^{10}$ Pa in our case). For $\eta = 1$, the conventional uniform stress drop $\Delta\sigma_0$ is a minimum estimate of the average stress drop weighted by the dislocation distribution on the fault plane (Kikuchi & Fukao 1988). The quasi-static solution for a radially expanding crack (Sato & Hirasawa 1973) gives $\eta \sim (v/V_S)^2$ ($\eta \sim 0.7$ in our case). The highest value of $\overline{\Delta\sigma}$ corresponds to Brune's (1970) stress drop $\Delta\sigma_B$ ($\eta = 0.46$; Kikuchi & Fukao 1988). The application of eq. (3) gives $\Delta\sigma_0 \sim 41$ bars, $\overline{\Delta\sigma} \sim 59$ bars, $\Delta\sigma_B \sim 90$ bars.

In summary, considering the quasi-static solution of Sato & Hirasawa (1973) for an expanding circular crack, we propose that the Lorient earthquake ruptured over a circular fault surface about 410 m in radius at a depth of 12.5 km. According to the definition of the scalar seismic moment $M_0 = \mu\Delta_U A$ (Aki 1967), the average co-seismic displacement Δ_U was large ($\sim$15 cm), and associated with a high stress drop (60 bars). The large amount of energy radiated in seismic waves also suggests that the stress release was complete, with only a small amount of energy dissipated by friction processes. In the following days, the stresses induced around the rupture area were released up to 1 km away from the main shock hypocenter.

4.4 Magnitudes

Magnitudes are computed using the formula of Lee *et al.* (1972):

$$M_l = 0.087 + 2\log(coda) + 0.0035\Delta,$$

where *coda* is the duration of the signal in second, and Δ, the epicentral distance in kilometres. The magnitude range goes from 0.4 to 1.9, with 17 events which have a magnitude lower than 1. This exceptional detection of low magnitude events could be explained by the absence of a thick sedimentary layer. We are able to check the magnitude only for the event occurring on October 2 at 23h33 as, after this date, the energy of the aftershocks was too low to be recorded by a sufficient number of LDG network stations allowing the source parameters processing. We compute a magnitude $M_l = 1.9$ and the LDG provides a magnitude $M_l = 2.0$ for the same earthquake, which gave us some confidence in the Lee *et al.*'s (1972) formula for this sequence.

4.5 Fault plane solutions

We use *P* wave polarities to build fault planes solutions of the aftershocks using FOCMEC routine (Snoke *et al.* 1984). From the 49 events inside the network, 34 fault plane solutions are computed. Due to the central location of the aftershocks main swarm with respect to the network geometry (Fig. 7), the focal mechanism processing has not been disturbed by any azimuthal coverage gap, as shown by the polarity distribution on most of the computed solutions (Fig. A1). The FOCMEC routine computes all possible double-couple solutions given the sense of the polarities. The solutions displayed in Fig. A1 are in agreement with all the polarities available for each event (Table A1). For two events, it is difficult to find a fault plane solution (box in Fig. A1). Finally, 32 solutions are selected (Tables 3 and A1) and a conservative quality factor has been defined for these solutions following the strike uncertainties (see Appendix A).

The majority of the nodal plane solutions shows strike-slip mechanisms with a normal component in good agreement with the general seismotectonic pattern of the SASZ and with the solution of the main

Table 3. Location and fault plane parameters of the 32 selected events.

Number	Day	Hour	Longitude (°)	Latitude (°)	Depth (km)	Mag.	Plane			Quality factor
							Str. (°)	Dip (°)	Slip (°)	
1	2	15:34	−3.163	47.845	12.7	0.6	16.00	76.00	5.00	4
2	2	20:58	−3.161	47.846	12.9	0.4	307.07	71.96	−161.04	4
3	2	21:04	−3.163	47.845	12.9	0.6	258.65	80.01	177.97	4
4	2	23:09	−3.165	47.849	12.1	0.7	282.97	32.10	−109.80	1
5	2	23:33	−3.176	47.854	12.2	1.9	100.00	86.00	−170.00	3
6	3	03:23	−3.152	47.869	14.3	0.6	160.00	81.00	−5.00	4
7	3	03:30	−3.162	47.846	13.2	1.2	130.35	88.03	−169.99	3
8	3	05:55	−3.172	47.853	12.0	0.6	206.00	68.00	28.00	2
9	3	07:55	−3.164	47.846	12.8	0.6	123.54	58.67	−119.54	1
10	3	09:24	−3.164	47.850	11.9	0.7	221.00	85.00	30.00	4
11	3	13:02	−3.177	47.853	12.2	1.4	346.00	63.00	−38.00	3
12	3	13:32	−3.161	47.846	13.3	1.2	250.00	90.00	180.00	4
13	3	19:51	−3.172	47.851	11.7	0.8	180.01	44.00	−22.00	2
14	3	20:56	−3.169	47.846	11.9	1.2	212.00	77.00	16.00	4
15	3	23:12	−3.152	47.853	14.2	1.3	263.73	75.00	178.96	4
16	3	23:50	−3.154	47.843	12.6	0.9	115.95	80.44	−162.75	3
17	4	00:52	−3.153	47.854	13.9	1.1	264.27	70.01	177.87	4
18	4	03:46	−3.181	47.853	12.1	0.8	112.31	69.65	−165.05	4
19	4	13:38	−3.165	47.832	13.4	0.9	69.91	70.03	176.81	3
20	4	15:38	−3.179	47.853	12.6	1.5	359.00	79.00	−10.00	4
21	5	14:03	−3.160	47.845	13.0	1.5	131.26	60.00	−125.26	1
22	5	20:59	−3.165	47.843	12.9	0.9	120.52	46.83	−166.23	3
23	6	02:49	−3.173	47.854	11.9	1.7	201.31	85.02	29.62	2
24	8	03:23	−3.166	47.847	12.6	1.0	172.00	40.00	−6.00	3
25	8	08:39	−3.165	47.847	12.7	0.7	305.07	71.96	−161.04	4
26	8	10:51	−3.165	47.848	12.7	1.9	127.19	65.44	−128.97	1
27	9	22:58	−3.170	47.848	13.1	1.4	222.00	83.00	29.00	4
28	10	12:06	−3.166	47.847	12.9	0.7	309.52	62.00	−158.12	1
29	10	23:21	−3.166	47.847	13.2	0.8	157.00	46.00	−54.00	2
30	12	03:10	−3.158	47.842	12.7	1.4	119.90	67.50	−133.59	1
31	12	05:11	−3.173	47.851	12.1	0.6	343.00	57.00	−40.00	3
32	12	23:36	−3.156	47.847	12.8	0.9	146.80	56.97	−113.97	1

The event numbers refer to the text and to Figs 8 and 9. Magnitudes are M_l magnitudes computed using the formula of Lee *et al.* (1972). The nodal plane is the one selected from the inversion (Fig. 10). Strike (Str.), Dip and Slip are given according to Aki & Richards (1980). The quality factor goes from 1 to 4, with a value of 1 for the poorly constrained solutions. See Appendix A for details.

Table 4. Values of $\sigma 1$, $\sigma 2$, $\sigma 3$ and R obtained from the inversion of the fault plane solutions determined in this study.

n	$\sigma 1$		$\sigma 2$		$\sigma 3$		R
	st. (°)	plg.(°)	st. (°)	plg.(°)	st. (°)	plg.(°)	
32	321.9 ± 9.6	15.3 ± 24.4	139.2 ± 59.3	74.7 ± 24.4	231.7 ± 10.1	0.7 ± 15.r1	0.60 ± 0.30
24	317.9 ± 4.3	7.2 ± 12.3	159.9 ± 46.4	82.2 ± 11.6	48.3 ± 2.9	2.9 ± 5.0	0.69 ± 0.14

n is the number of focal mechanisms used. σ_1, σ_2 and σ_3 are the maximum values of the principal stresses, respectively. R is the stress ratio $= \frac{\sigma_2-\sigma_3}{\sigma_1-\sigma_3}$. St and Pl are the strike and the plunge of each principal stress component.

shock (Fig. 8). One of the largest events (26) shows a normal fault solution with a dextral strike-slip component, similar to the one of the main shock. A possible fault plane for these solutions is close to the direction of SASZ with a direction of the rupture plane around N120°.

The A1B1 cross-section (Fig. 9) brings information on the displacements related to the 2 clusters on the fault plane: the lower cluster depicts normal faulting whereas the upper one shows mainly strike-slip focal mechanisms. The A2B2 cross-section (Fig. 9) underlines a general trend of the aftershocks with a nodal plane dipping 60° ± 5° to the south. Event 12 has a different focal mechanism: its marginal position (almost at the lower eastern corner of the fault plane with the deepest location) suggests to consider it separately from the other focal mechanisms.

All together, nodal planes and hypocenters favour a 60° SW dipping fault plane striking N120° between 12 and 13.5 km depth. This fault geometry deduced from the aftershock analysis is in good agreement with the source parameters obtained for the main shock (strike 117°, dip 62° and rake −133°). The rupture may have nucleated in the lower part the fault and then have propagated upwards in the NW direction. Nodal planes located in the upper northwestern corner tends to strike more in the N–S or in the E–W directions.

4.6 Stress tensor deduced from focal mechanisms

The 32 focal solutions have been combined in order to determine a stress tensor solution using the inversion method of Etchecopar *et al.* (1981). Etchecopar's method is a numerical inversion method

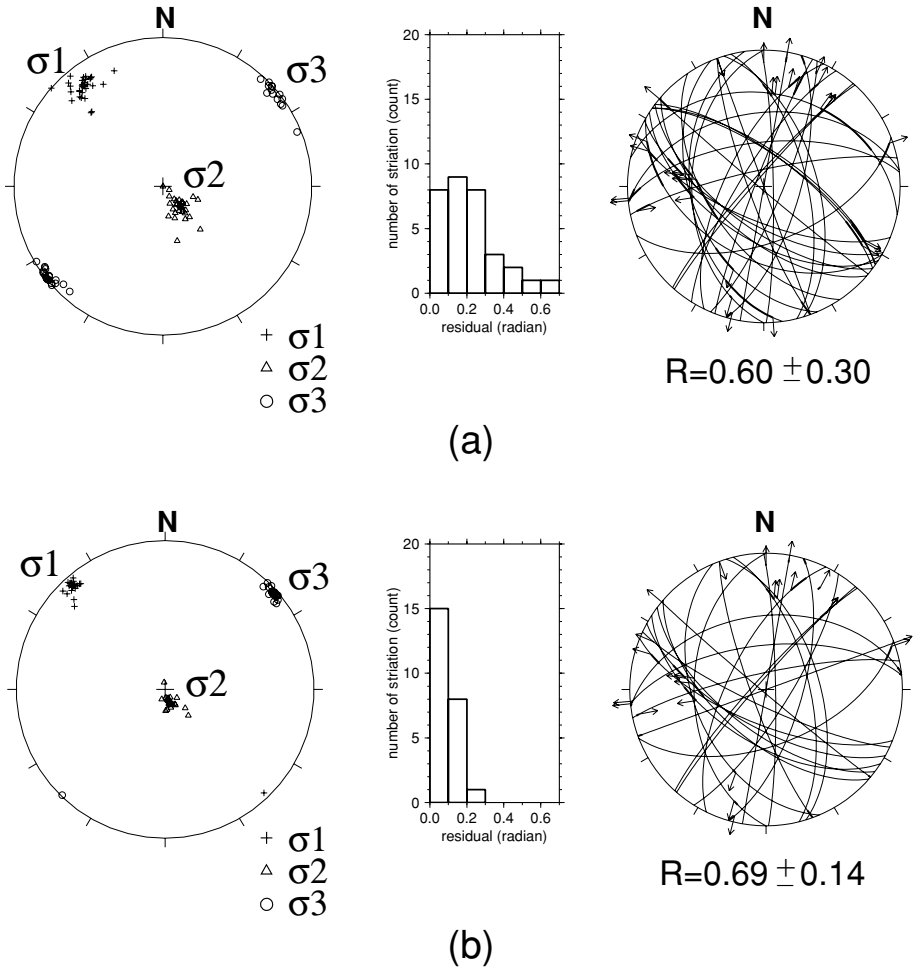

Figure 10. Lower-hemisphere projection of the stress tensor computed using the fault plane solutions listed in Table 3. The fault planes selected by the numerical method (Etchecopar *et al.* 1981) are also represented. The misfit between observed (arrows) and computed slip vectors is drawn with heavy solid curves. The histograms show the resulting angular deviations (residuals) between observed and computed slip vectors. R is the stress ration with $R = (\sigma_2 - \sigma_3)/(\sigma_1 - \sigma_3)$. a) All 32 focal mechanisms used; b) data subset eliminating the 8 less constrained focal mechanisms.

which allows us to compute the components of the stress tensor as well as the stress ratio $R = (\sigma_2 - \sigma_3)/(\sigma_1 - \sigma_3)$, where σ_1, σ_2 and σ_3 are the maximum, intermediate and minimum principal stress values, respectively, thus allowing for an interpretation of the stress regime. It minimizes the sum of the angular differences between the theoretical fault plane predicted from some trial tensor and the observed one, and it finally provides the estimated errors for the deduced stress tensor components and for the R ratio. The quality factor for the fault plane (Table 3) is the weighting factor in the inversion procedure. In a first run, no focal mechanism needs to be rejected because the inversion converges with a good misfit function for all fault plane solutions (Table 4). In a second step, the eight focal mechanisms which present the highest misfit function in the first approach are rejected. The latter mechanisms are also less well constrained than the 24 remaining ones. This last step provides similar values for σ_1 (Fig. 10) but minimizes the errors on the axes direction and on the value of the stress ratio R (Table 4). It confirms the first results found using the whole data set (Fig. 10). We made several trials varying the number of trial tensors and the way to generate tensors, but the different trials converged to similar results within the estimated errors (Table 4).

The fault planes selected in the inversion procedure are listed in Table 3. We clearly identify on a plot (rose diagram) of strikes of nodal planes (Fig. 2) a maximum around N120°, in good agreement with the azimuth of the SASZ southern branch and with the focal mechanism of the main shock. The N–S and N30° Hercynian directions are also visible but concern a smaller number of nodal planes. Looking at the events with the largest magnitudes (Fig. 8), the selected fault planes for the solutions 21, 26 and 30 confirm the direction and the dip of the main shock (fault planes striking around N120° and dipping 60° SW). These mechanisms depict a rupture similar to the Lorient earthquake and are located in the eastern lower part of A1B1 Section (Fig. 9). In the same area, a little bit deeper, Event 7 shows a nodal plane striking N130° which is nearly vertical suggesting some reactivation of the southern branch of the SASZ.

For the NW group of the largest events (5, 11, 20 and 23, Fig. 8), the inversion is favoured by the north–south plane direction. These events are located in the upper western part of the aftershock area. These aftershocks could be located on another fault plane striking N–S as already indicated by the morphological analysis of the region. This north–south fault may be part of a complicated source rupture or may have played back as a response to the stress change following the main shock. Other most significant fault plane solutions (12, 14, 27, Fig. 8) have a smaller magnitude and are, therefore, difficult to link with surface trends.

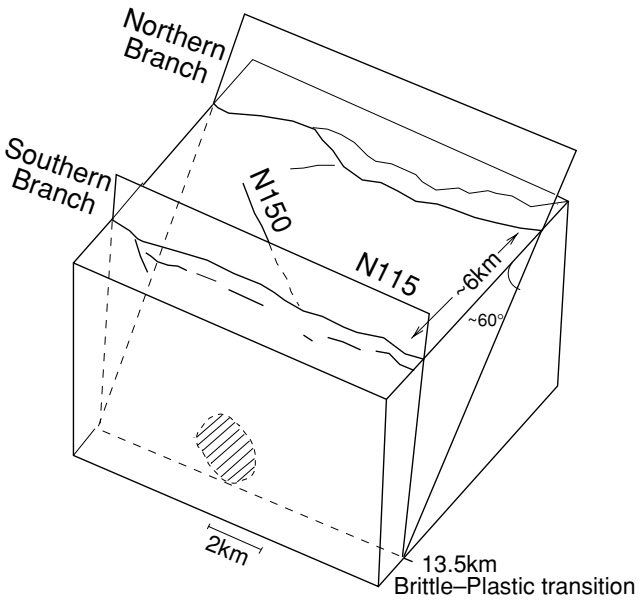

Figure 11. A 3-D tectonic sketch of the area around the fault which may have been activated during the Lorient earthquake. the circular dashed area shows the aftershocks distribution.

Our stress inversion results into a strike-slip tectonic regime (Fig. 10) with σ_1 and σ_3 striking N317° ± 4.3° and N 48° ± 4.5°, respectively (Table 4). These directions and stress tensor are quite consistent with previous studies led at a more regional scale (Nicolas *et al.* 1990; Amorèse *et al.* 2000). In this stress regime, the SW dipping nodal plane of the Lorient earthquake should play with a dominant normal component, which is indeed observed (Fig. 8). Following the classification from Ritz (1994), the value of the stress ratio $R = 0.69 \pm 0.14$ is at the limit which separates a pure strike-slip regime from a transtensive one, with σ_2-axis getting closer to σ_1 and confirming the two main characteristics of the data set of focal mechanisms. This result differs from the one proposed by Mazabraud *et al.* (2005) in the South Armorican Massif, who found an extensional stress regime based on seven fault plane solutions.

5 DISCUSSION AND CONCLUSIONS

In an attempt to interpret these results in terms of fault rupture, we consider three scenarios:

(1) the rupture nucleated on the eastern part of the aftershock zone and then propagated up in the western direction and jumped to another north-south segment,

(2) the rupture area of the main shock occurred at 13 km and is represented by the lower east aftershock cluster or

(3) the rupture occurs in the middle of the two clusters at 12.5 km and the aftershocks are located at the boundaries of the rupture zone. The first scenario may require much more energy than a Mw = 4.3 earthquake. Moreover, we did not manage to model the broadband waveforms using two different point sources to simulate the rupture. In the second scenario, the rupture has nucleated at 13-km depth in the eastern part of the aftershock area. Owing to the stress perturbation, a north-south fault segment located at 12 km in the western part has been activated. In this scenario, the Lorient earthquake should have broken a rupture zone of 0.5-km radius at 13-km depth with a stress drop of ≈90 bars, which is not compatible with the corner frequency. The third scenario is the most probable one: the rupture occurs at 12.5 km, in the area without aftershock (Fig. 9), with a stress drop of about 60 bars and a 0.5-km radius rupture. Then the rupture propagated up to NW and down to SE until it reaches the brittle/ductile boundary. In this scenario, the aftershocks are located at the limits of the rupture zone where the stress induced by the Lorient earthquake is released. This active fault can be related to the prolongation at depth of the SASZ northern branch located 6 km away from the aftershock area (Fig. 11). The northern branch of the SASZ is then interpreted as a south dipping N60° fault probably connected at depth to the subvertical southern branch of the SASZ (Figs 2 and 11).

The DEM and field analysis allow us to identify two main directions in the Lorient area: the ≈N–S and the E–W to N120° trending structures. As the aftershock fault plane solutions show the same directions, it implies a strong structural inheritance of the area, dominated by Hercynian structures which are reactivated by the current stress regime. As no evidence of recent deformations have been found at the surface and as the magnitudes of the events in the Armorican massif is low to moderate, we may assume that the present-day strike-slip stress field is not active enough to leave a clear print up to the surface. The current stress tensor operates only at the deep parts of the pre-existing faults because fault instabilities are increasing with depth (Scholz 1990), permitting deformations even at low stress regime. This interpretation is supported by the fact that the largest recorded earthquakes in the Armorican Massif generally occurred at or below 10-km depth, probably at the limit between the brittle and ductile crust. Moreover the focal mechanisms on the SASZ (Fig. 1) present dipping fault planes, which do not need as much stress as the vertical strike-slip to be reactivated (Scholz 1990).

The deduced NW–SE compressional stress and NE–SW extensional stress are in good agreement with previous regional studies (Nicolas *et al.* 1990) and with the more detailed study in the northern part of the Armorican Massif (Amorèse *et al.* 2000). Noting that all previous studies have determined stress fields using several focal mechanisms over large areas, our stress field is still able to depict the regional trend, suggesting a rather large-scale stress source. The NW–SE σ_1-axis can be explained by two mechanisms: the ridge push from the mid-Atlantic ridge system and the Alpine compression (Gölke & Coblentz 1996). Both explanations are possible and together can be the cause of the current NW–SE strike-slip stress tensor. Since our stress field is strike-slip with a tendency for extension (Delouis *et al.* 1993), it means that another source of stress should be added vertically. It could be found in buoyancy forces arising since the deglaciation, thus explaining the general observed uplift in Brittany (Bonnet *et al.* 1998, 2000).

This study shows that undertaking a post-seismic survey for moderate-size earthquakes is fruitful in many aspects. Indeed, the SISBREIZH campaign allows us to locate 62 aftershocks and to compute numerous fault plane solutions following the 2002 September 30, Lorient earthquake. This effort has provided a new data set which is important to understand the seismic activity of an intraplate area such as the Armorican Massif.

ACKNOWLEDGMENTS

The authors thank the French INSU-CNRS for providing financial support to undertake and to process the data of the SISBREIZH campaign. We are grateful to all the people involved in the running of the INSU portable seismic network, especially Jean Claude Lépine

and Jean Verhille of IPG in Paris for the quick forwarding of the seismic stations. PA benefits from a doctoral grant of the Conseil Régional des Pays de la Loire. Contribution N°956 of the IUEM, European Institute for Marine Studies (Brest, France).

REFERENCES

Aki, K., 1967. Scaling law of seismic spectrum, *J. geophys. Res.,* **72,** 1217–1231.

Aki, K. & Richards, P.G., 1980. *Quantitative Seismology: Theory and Methods,* W.H. Freeman and Co., San Francisco.

Amorèse, D., Walker, A., Lagarde, J.-L., Santoire, J.-P., Volant, P., Font, M. & Lecornu, M., 2000. New seismotectonic data from an intraplate region: focal mechanisms in the Armorican Massif (northwestern France), *Geophys. J. Int.,* **143,** 837–846.

Ballèvre, M., Marchand, J., Godard, G., Goujou, J. & Wyns, R., 1994. Eo-Hercyninan events in the Armorican Massif, in *Pre-Mesozoic Geology in France and Related Areas,* pp. 183–194, ed. Keppie, J., Springer Verlag, Berlin.

Bonner, J.L., Delaine, T.R. & Shumway, R.H., 2002. Application of a cepstral F-statistic for improved depth estimation, *Bull. seism. Soc. Am.,* **92,** 1675–1693.

Bonnet, S., 1997. *Tectonique et dynamique du relief: le socle armoricain au Pléistocène,* thèse de l'Université de Rennes I, Mémoire de Géosciences Rennes, **86,** 352 pp.

Bonnet, S., Guillocheau, F., Brun, J.-P. & Van Den Driessche, J., 2000. Large-scale relief development related to Quaternary tectonic uplift of a Proterozoic-Paleozoic basement: the Armorican Massif, nw France, *J. geophys. Res.,* **105,** 19 273–19 288.

Bouchon, M., 1981. A simple method to calculate Green's functions for elastic layered media, *Bull. seism. Soc. Am.,* **71,** 959–971.

Brun, J.-P. & Bale, P., 1990. Cadomian tectonics in northern Brittany, in *Cadomian Orogeny,* Vol. 51, pp. 95–114, eds Strachan, R.A., Topley, C.G. & D'Lemos, R.S., Geol. Soc. Spec. Publ.

Brun, J.-P. & Burg, J.-P., 1982. Combined thrusting and wrenching in the Ibero-Armorican arc, *Earth planet. Sci. Lett.,* **61,** 319–332.

Brune, J., 1970. Tectonic stress and spectra of seismic shear waves from earthquakes, *J. geophys. Res.,* **75,** 4997–5009, Correction, 1971. *J. geophys. Res.,* **76,** 5002.

Courboulex, F., Deichmann, N. & Gariel, J.-C., 1999. Rupture complexity of a moderate intraplate earthquake in the Alps: the 1996 M5 Epagny-Annecy earthquake, *Geophys. J. Int.,* **139,** 152–160.

Delouis, B., Haessler, H., Cisternas, A. & Rivera, L., 1993. Stress tensor determination in France and neighbouring regions, *Tectonophysics,* **221,** 413–437.

Etchecopar, A., Vasseur, G. & Daignieres, M., 1981. An inversion problem in microtectonics for the determination of stress stensors from fault striation analysis, *J. Struct. Geol.,* **3,** 51–65.

Gölke, M. & Coblentz, D., 1996. Origins of the European regional stress field, *Tectonophysics,* **226,** 11–24.

Gros, Y. & Limasset, O., 1984. Dèformations rècentes dans le socle cristallin: exemple du Massif Armoricain, rapport 84, BRGM (Bureau de Recherches Géologiques et MiniËres).

Gutenberg, B. & Richter, C., 1956. Earthquake Magnitude, intensity, energy and acceleration, *Bull. seism. Soc. Am.,* **46,** 105–145.

Haskov, J. & Ottemöller, L., 1999. SEISAN earthquake analysis software, *Seism. Res. Lett.,* **70,** 532–534.

Jegouzo, P., 1980. The South Armorican Shear Zone, *J. Struct. Geol.,* **2,** 39–47.

Judenherc, S., Granet, M., Brun, J.-P., Poupinet, G., Plomerová, J., Mocquet, A. & Achauer, U., 2002. Images of lithospheric heterogeneities in the Armorican segment of the Hercynian range in France, *Tectonophysics,* **358,** 121–134.

Kanamori, H., 1977. The energy release in great earthquakes, *J. geophys. Res.,* **82,** 2981–2987.

Kennett, B., 1991. *IASPEI 1991 Seismological Tables,* Bibliotech, Canberra, Austrlia.

Kikuchi, M. & Fukao, Y., 1988. Seismic wave energy inferred from long-period body wave inversion, *Bull. seism. Soc. Am.,* **78,** 1707–1724.

Klein, F., 1984. Users guide to HYPOINVERSE, a program for Vax and PC350 computers to solve for earthquake locations. Open File Report 84-000, US Geological Survey.

Lee, W.H.K., Bennet, R.E. & Meagher, L., 1972. A method for estimating magnitude of local earthquakes from signal duration, Open file report, U.S.G.S.

Lenôtre, N., Thierry, P. & Blanchin, R., 1999. Current vertical movement demonstrated by comparative leveling in Brittany (northwestern France), *Tectonophysics,* **301,** 333–344.

Lienert, B.R.E., Berg, E. & Frazer, L.N., 1986. Hypocenter: An earthquake location method using centered, scaled, and adaptively damped least squares, *Bull. seism. Soc. Am.,* **76,** 771–783.

Madariaga, R., 1976. Dynamics of an expanding circular fault, *Bull. seism. Soc. Am.,* **66,** 639–666.

Mazabraud, Y., Béthoux, N., Guilbert, J. & Bellier, O., 2005. Evidence for short scale field variations within intraplate central-western France, in press *Geophys. J. Int.*, **160,** 161–178.

Montadert, L. *et al.* 1977. Rifting and subsidence on passive continental margins in the North-East Atlantic, *Nature,* **268,** 305–309.

Nicolas, M., Santoire, J.P. & Delpech, P.Y., 1990. Intraplate seismicity: new seismotectonic data in Western Europe, *Tectonophysics,* **179,** 27–53.

Rabu, D., Chantraine, J., Chauvel, J.-J., Denis, E., Bale, P. & Bardy, P., 1990. The Brioverian (Upper Proterozoic) and the Cadomian Orogeny in the Armorican Massif, in *Cadomian Orogeny,* Vol. 51, pp. 81–94, eds Strachan, R.A., Topley, C.G. & D'Lemos, R.S., Geol. Soc. Spec. Publ.

Reasenberg, P.A. & Oppenheimer, D., 1985. FPFIT, FPPLOT and FPPAGE: Fortran computer programs for calculating and displaying earthquake fault-plane solutions, Open file report 85-739, US Geological Survey.

Ritz, J.-F., 1994. Determining the slip vector by graphical construction: use of a simplified representation of the stress tensor, *J. Struct. Geol.,* **16,** 737–741.

Rolet, J., 1994. The Armorican Massif, Structure and Metamorphism, Introduction, in *Pre-Mesozoic Geology in France and Related Areas,* pp. 177–178, ed. Keppe, J., Springer Verlag, Berlin.

Sato, T. & Hirasawa, T., 1973. Body wave spectra from propagating shear cracks, *J. Phys. Earth,* **21,** 415–431.

Scholz, C., 1990. *The mechanics of earthquakes and faulting,* Cambridge Univ. Press, Cambridge, UK.

Shelley, D. & Bossière, G., 2000. A new model for the Hercynian Orogen of Gondwanan France and Iberia, *J. Struct. Geol.,* **22,** 757–776.

Shumway, R.H., 1971. On detecting a signal in N stationarily correlated noise series, *Technometrics,* **10,** 523–534.

Snoke, J.A., Munsey, J.W., Teague, A.G. & Bollinger, G.A., 1984. A program for focal mechanism determination by combined use of polarity and SV-P amplitude ratio data, *Earthquake notes,* **55,** 15.

Vassiliou, M. & Kanamori, H., 1982. The energy release in earthquakes, *Bull. seism. Soc. Am.,* **72,** 371–387.

Vigneresse, J., 1988. La fracturation post-hercynienne du Massif Armoricain d'après les données géologiques, *Géol. Fr.,* **4,** 3–10.

Waldahauser, F. & Ellsworth, W.L., 2000. A double-difference earthquake algorithm: method and application to the northern Hayward fault, *Bull. seism. Soc. Am.,* **90,** 1353–1368.

Wyns, R., 1991. Evolution tectonique du bâti armoricain oriental au Cénozoïque d'après l'analyse des paléosurfaces continentales et des formations géologiques associées, *Géol. Fr.,* **3,** 11–42.

Ziegler, P.A., Cloething, S. & van Wees, J.-D., 1995. Dynamics of intraplate compressional deformation: the Alpine foreland and other examples, *Tectonophysics,* **252,** 7–59.

APPENDIX A: FAULT PLANE SOLUTIONS

The FOCMEC routine computes all possible fault planes solutions. The uncertainty on the strike and dip of the plane is the difference between the minimum and the maximum values found among the possible fault planes of a same family. When several families of fault

Table A1. Parameters used for the location and focal mechanism processes.

n	nP_g	nS_g	*npol*	Δ Strike (°)	Δ Dip (°)	Quality factor
1	11	11	11	18.0	12.0	4
2	6	9	6	1.0	1.0	4
3	8	11	8	11.0	10.0	4
4	10	8	10	70.0	20.0	1
5	13	12	13	21.0	13.0	3
6	10	10	10	11.0	18.0	4
7	12	11	11	23.0	15.0	3
8	7	10	7	30.0	12.0	2
9	8	10	8	47.0	26.0	1
10	12	11	12	7.0	7.0	4
11	11	11	10	27.0	20.0	3
12	11	11	11	11.0	2.0	4
13	12	9	12	30.0	13.0	2
14	13	12	13	11.0	12.0	4
15	12	12	12	16.0	5.0	4
16	9	8	9	21.0	19.0	3
17	12	9	12	11.0	7.0	4
18	12	12	12	11.0	7.0	4
19	10	10	10	21.0	18.0	3
20	13	13	13	10.0	9.0	4
21	11	11	11	56.0	40.0	1
22	10	9	10	22.0	15.0	3
23	10	7	10	30.0	15.0	2
24	8	9	9	20.0	30.0	3
25	9	8	9	2.0	1.0	4
26	11	10	11	62.0	70.0	1
27	11	9	11	1.0	5.0	4
28	6	8	6	37.0	20.0	1
29	8	10	8	35.0	43.0	1
30	11	10	11	64.0	42.0	1
31	8	9	8	20.0	13.0	3
32	10	10	9	53.0	35.0	1

n is the event number, nP_g and nS_g are the number of picked phases per event for *P* and *S* waves, respectively. *npol* is the number of polarity used to determine the focal mechanisms. Δ Strike and Δ Dip are the ranges between the minimum and maximum value obtained for the strike and the dip of all the possible fault planes. The quality factor indicates the validity of the solution as defined above in this section.

planes are present, the larger value is kept. From these uncertainties, we establish a quality factor per event (Table A1) following:

4: $\Delta Str < 20^\circ$ and $\Delta Dip < 20^\circ$(13 events)
3: $20 \leq \Delta Str < 30^\circ$ (8 events)
2: $30 \leq \Delta Str < 35^\circ$ (3 events)
1: $\Delta Str \geq 35^\circ$ with first motion amplitudes control (8 events)

If the value of the quality factor is greater than 2, there is no difficulty to select a solution among the possible plane. For the event with a quality factor equal to 1, we select the fault plane according to the relative amplitude of the first motion data. Only two events are rejected because they present too many different solutions (see box in Fig. A1).

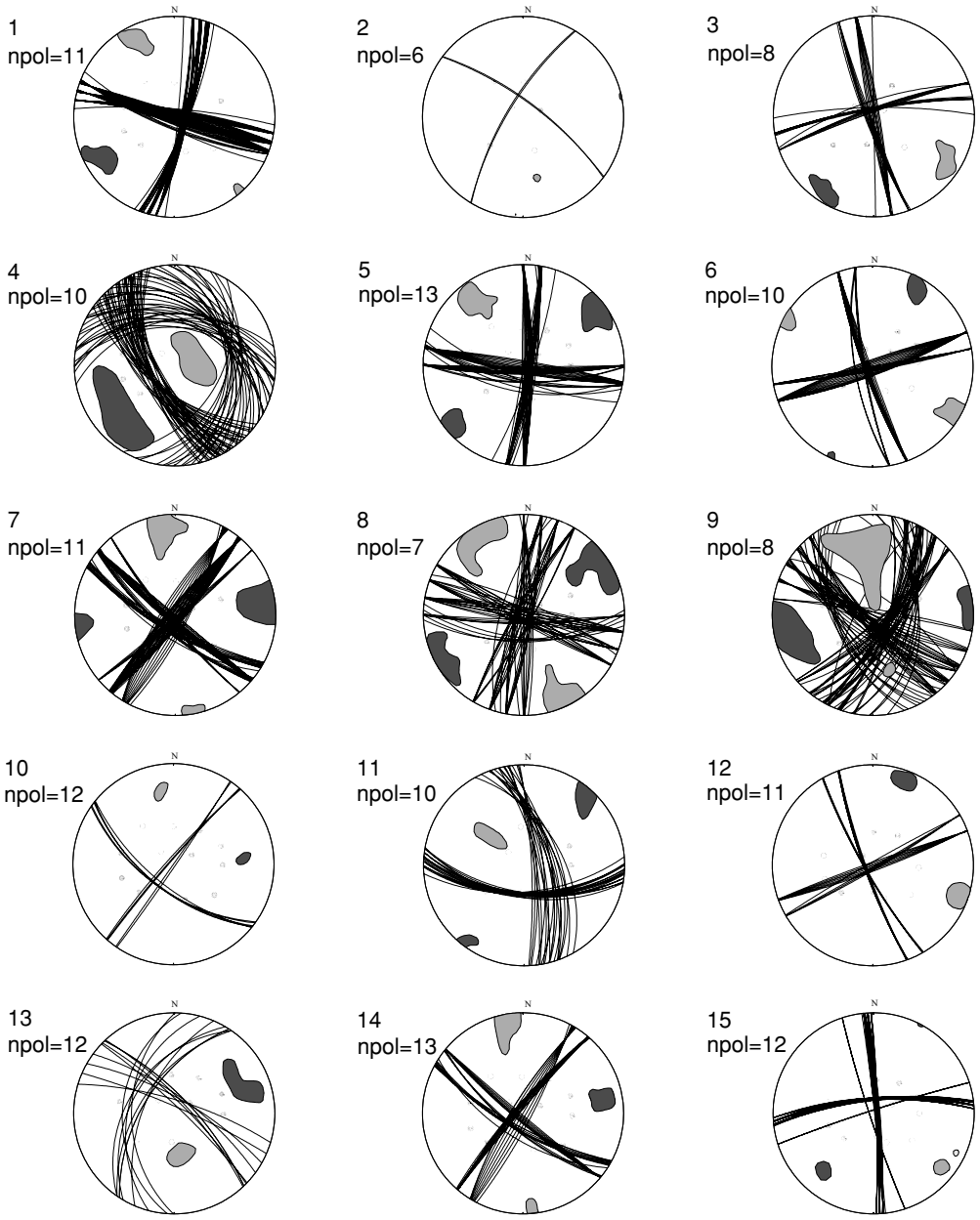

Figure A1. Fault plane solutions of the aftershocks. Each possible fault plane is displayed per event, the number on the upper left side of the beach ball is referring to the event listed in Table 3. Black and white dots represent the compressional and dilatational polarities, respectively. npol is the number of polarities. The light and dark grey areas represent the *P*- and *T*-axis domains, respectively. Two unconstrained rejected solutions are displayed in the box at the bottom of the figure.

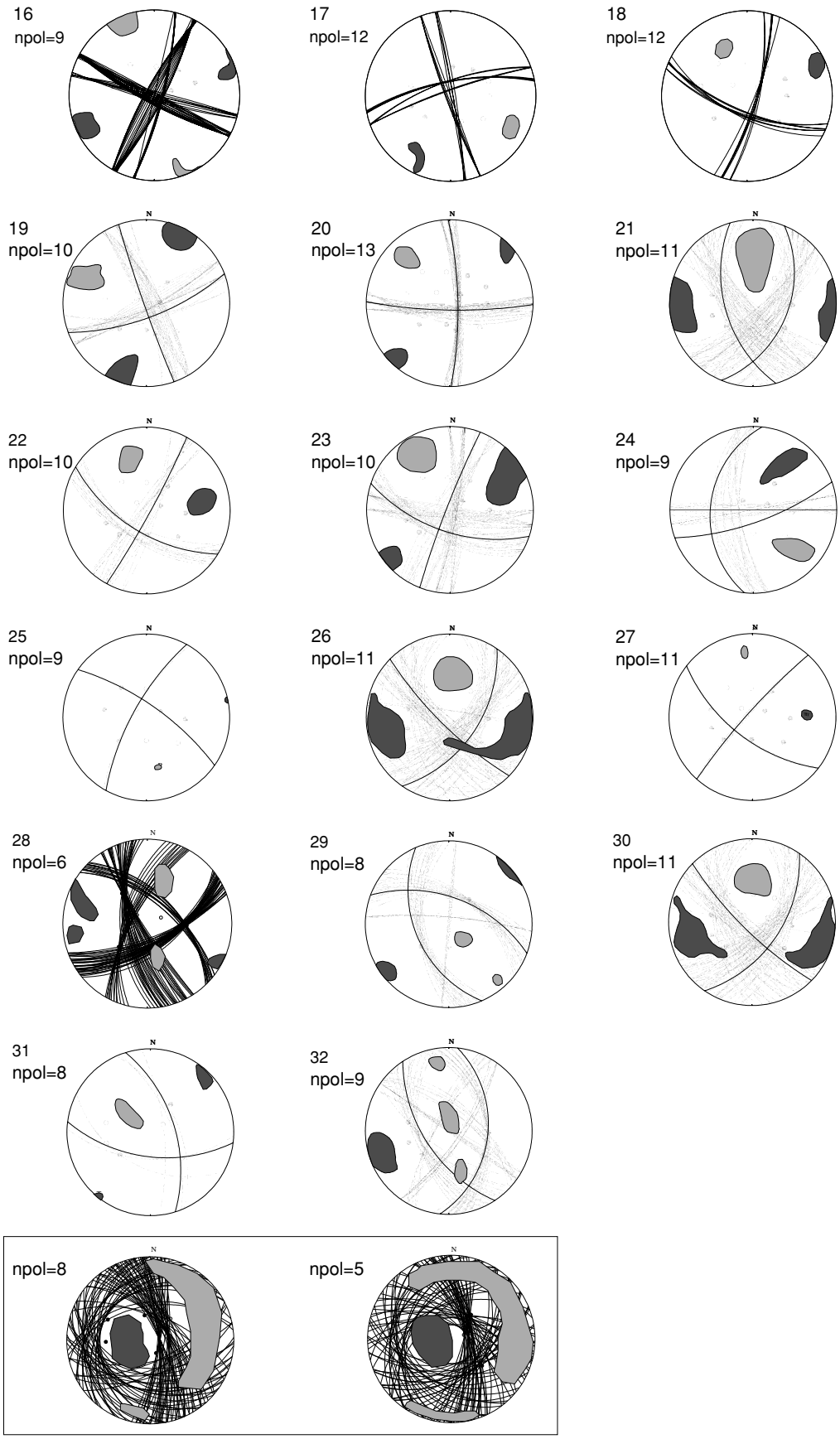

Figure A1. (*Continued*.)